

Electrodeposited Ni-based magnetic mesoporous films as smart surfaces for atomic layer deposition: an ‘all-chemical’ deposition approach toward 3D nanoengineered composite layers

Jin Zhang^{1,2,}, Alberto Quintana¹, Enric Menéndez¹, Mariona Coll³, Eva Pellicer^{1,*}, Jordi Sort^{1,4,*}*

¹Departament de Física, Facultat de Ciències, Universitat Autònoma de Barcelona, E-08193 Bellaterra, Cerdanyola del Vallès, Spain

²State Key laboratory of Solidification Processing, Center of Advanced Lubrication and Seal Materials, Northwestern Polytechnical University, Xi'an, Shaanxi, 710072, P. R. China

³Institut de Ciència de Materials de Barcelona (ICMAB-CSIC) Campus UAB, E-08193 Bellaterra, Catalonia, Spain

⁴Institució Catalana de Recerca i Estudis Avançats (ICREA), Pg. Lluís Companys 23, E-08010 Barcelona, Spain

KEYWORDS: mesoporous films, nanoengineered composites, surfactant-assisted electrodeposition, atomic layer deposition, magnetic properties.

ABSTRACT

Mesoporous Ni and Cu-Ni ($\text{Cu}_{20}\text{Ni}_{80}$ and $\text{Cu}_{45}\text{Ni}_{55}$ in at. %) films, showing a three-dimensional (3D) porous structure and tunable magnetic properties, are prepared by electrodeposition from aqueous surfactant solutions using micelles of P-123 tri-block copolymer as structure-directing entities. Pores between 5 nm and 30 nm and dissimilar space arrangements (continuous interconnected networks, circular pores, corrugated mesophases) are obtained depending on the synthetic conditions. X-ray diffraction studies reveal that the Cu-Ni films have crystallized in the face-centered cubic structure, are textured, and exhibit certain degree of phase separation, particularly those with a higher Cu content. Atomic layer deposition (ALD) is used to conformally coat the mesopores of $\text{Cu}_{20}\text{Ni}_{80}$ film with amorphous Al_2O_3 , rendering multiphase “nano-in-meso” metal-ceramic composites without compromising the ferromagnetic response of the metallic scaffold. From a technological viewpoint, these 3D nanoengineered composite films could be appealing for applications like magnetically-actuated micro/nano-electromechanical systems (MEMS/NEMS), voltage-driven magneto-electric devices, capacitors or as protective coatings with superior strength and tribological performance.

1. Introduction

Mesoporous metallic materials with high electroconductivity and surface area have sparked much attention during recent years owing to their wide range of applications in areas such as electronic devices, catalysis, energy technologies or even recording media¹. Their intrinsically porous structure has proven to be useful for the adsorption, selection, sensing, removal, storage and release of second-phase materials²⁻⁷. Given their large potential, several techniques have been developed during the last decades in order to controllably create nanoporosity, either by selective etching from the fully dense counterparts (*e.g.*, dealloying or foaming)⁸⁻⁹ or spontaneous association of small building blocks while leaving empty spaces in between (bottom-up approach)¹⁰⁻¹². From the viewpoint of material's architecture, control of the alloy composition needs to be often combined with precise tailoring of the mesoporous morphology, pore alignment, and orientation. This still remains a challenging issue. Most approaches rely on relatively slow, multi-step synthetic procedures, sometimes including costly clean room facilities. Ideally, such materials should be synthesized in a series of easy steps (preferably in a single- or two-step) allowing for a simple but precise control of the shape and morphology of the obtained structures.

During the last few years, mesoporous metals and alloys have been extensively prepared by means of sacrificial templates, using the replication method, from either soft or hard templates¹³⁻¹⁵. In the case of the templated deposition of metals, their growth from the substrate is guided by the template and the mesoporous structure often emerges after the template is removed. Very recently, the usage of spherical micelles of di- or tri-block copolymers (*e.g.*, polystyrene-block-poly(oxyethylene) (PS-b-PEO) known as KLE or Poly(ethylene glycol)-block-poly(propylene glycol)-block-poly(ethylene glycol) (PEG-PPG-PEG) known as P-123) in water as soft-templates has been demonstrated for a number of metals (*e.g.*, Au, Pt, Pd, Cu)¹⁶⁻¹⁹ and alloys (Pt-Cu, Pt-Ru,

Pt-Fe and Cu-Ni)²⁰⁻²⁴. Contrary to the evaporation-induced self-assembly approach, metal deposition and micelles assembly take place simultaneously in liquid phase without involving any solvent evaporation. Furthermore, because the concentration of the block copolymers is above the critical micelle concentration (cmc) but well below the threshold for the formation of lyotropic liquid crystal structures²⁵, the viscosity of the electrolyte does not dramatically increase.

The advances in the synthetic pathways to produce magnetic materials with different nanoarchitectures has boosted the discovery of new magnetic phenomena and, in turn, expanded the range of applications of magnetic materials, since many magnetic properties of materials rely on surface or interface phenomena²⁶. In this context, very recently, we demonstrated that magnetic mesoporous metallic materials, with an increased surface area-to-volume ratio, show enhanced magneto-electric phenomena compared to fully-dense films with analogous compositions²⁴. The system under study was Cu-Ni and mesoporous films of this alloy were successfully prepared by electrodeposition (ED) from ‘micelles assembly’ of P-123 in water. The coercivity of the as-prepared mesoporous Cu-Ni films could be drastically decreased by simply applying an external electric field. In our previous work, however, only the general features concerning the mesoporous organization for a particular Cu/Ni ratio were introduced. Instead, emphasis was laid on the electrically-driven modification of magnetic properties. The key experimental factors enabling the formation of the mesoporous structure were mostly overlooked.

Remarkably, besides the aforementioned magneto-electric effects, magnetic mesoporous metallic materials can also be successfully employed as supports to host other functional materials that could bring biocompatible, hydrophilic/hydrophobic properties, electrical insulation or even enhanced mechanical or magnetic performance²⁷. For example, 3D macroporous Ni films prepared by the hydrogen bubble templating approach can function as scaffolds to anchor electrodeposited

Co(OH)₂ nanoflakes or sputtered Si to produce nanoporous composites with superior supercapacitor and electrochemical performance^{28,29}. In the case of mesoporous materials of metallic nature, an appropriate technique should be carefully selected in order to conformally coat the mesopores with a second-phase material while avoiding or minimizing its oxidation and eventual pore collapse. Atomic layer deposition (ALD) turns out to be a powerful deposition technique that allows not only precise control over the composition of the deposited materials, but also these can continuously coat high aspect-ratio substrates³⁰⁻³². In fact, we proposed the combination of ED and ALD to prepare composite layers consisting of 3D macroporous magnetic metals coated with metal oxide nanolayers, *i.e.*, Ni/Al₂O₃, Ni/Co₂FeO₄³³. It was demonstrated that both the porosity and the magnetic properties of the electrodeposited metallic matrix were maintained after the ALD step under optimized ALD conditions. However, the ALD deposition was only tested on metallic films exhibiting large pore sizes, of the order of 5-15 μm. It was then envisaged that such synthetic approach could be well applied to out-of-sight surfaces of nanometric sizes (*e.g.*, mesopores) grown by surfactant-assisted ED.

In this work, Cu₂₀Ni₈₀, Cu₄₅Ni₅₅ and Ni magnetic mesoporous films are electrodeposited in the presence of P-123 tri-block copolymer dissolved in the aqueous electrolyte. The growth of mesoporous Ni coatings was carried out under potentiostatic mode, whereas Cu-Ni alloys were fabricated under galvanostatic means. Although all samples show mesoporosity, the resulting morphologies (*e.g.*, pore alignment) are different depending on the electroplating conditions. Insulating Al₂O₃, with a high dielectric constant, is chosen to coat the Cu₂₀Ni₈₀ framework (which is taken as a model) by means of ALD. The structure and magnetic properties of the films, before and after the ALD process, are studied in detail.

2. Experimental section

2.1. Synthesis of the Cu₂₀Ni₈₀, Cu₄₅Ni₅₅ and Ni magnetic mesoporous films

All the chemicals were purchased from Sigma-Aldrich and used without further purification. Electrochemical fabrication of nanoporous Ni and Cu-Ni films was carried out in a PGSTAT120N Autolab potentiationstat/galvanostat (Eco Chemie) with a standard three-electrode cell system. Si/Ti (25 nm)/Au (125 nm) substrates (working area 0.25 cm²) were used as cathode. A platinum wire served as counter electrode. The cathode and anode were mounted parallel to each other at a distance of 2 cm. A double junction Ag | AgCl 3 M KCl electrode ($E = + 0.210$ V versus standard hydrogen electrode (SHE)) was utilized as the reference electrode. The optimized growth parameters for the ED of nanoporous Ni, Cu₂₀Ni₈₀ and Cu₄₅Ni₅₅ are listed in Table 1. Note that due to the dissimilar deposition conditions (mainly the deposition time, which is different, but also other parameters like the bath formulation and deposition mode), the thickness of the mesoporous Ni film was measured to be around 7 μ m, whereas those of Cu₂₀Ni₈₀ and Cu₄₅Ni₅₅ were approximately 600 nm and 1 μ m, respectively. We anticipate that the thickness of the Cu richer film is probably a bit overestimated due to the influence of its higher roughness. Al₂O₃ nanolayers were deposited by ALD onto the previously electrodeposited porous metallic films in a Cambridge Nanotech Savannah 100 reactor in exposure mode. The Al₂O₃ coatings were produced by alternate pulsing of trimethylaluminum (TMA) and ozone (O₃) at a deposition temperature of 100-200 °C.

Table 1. Optimized electrodeposition parameters for the growth of mesoporous Ni, Cu₂₀Ni₈₀ and Cu₄₅Ni₅₅ films.

Mesoporous metallic film	Ni	Cu ₂₀ Ni ₈₀ (at. %)	Cu ₄₅ Ni ₅₅ (at. %)
Bath composition	0.08 g/mL P-123 20 mL ethanol 0.4 M NiSO ₄ 0.5 M NaSO ₄ 0.2 M boric acid 0.5 mg/mL saccharine	0.008 g/mL P-123 0.2 M Ni(OCOCH ₃) ₂ ·4H ₂ O 0.02 M CuSO ₄ ·5H ₂ O 0.5 M NaOCOCH ₃ 0.2 M boric acid 0.4 mg/mL saccharine	0.008 g/mL P-123 0.2 M Ni(OCOCH ₃) ₂ ·4H ₂ O 0.02 M CuSO ₄ ·5H ₂ O 0.5 M NaOCOCH ₃ 0.2 M boric acid 0.4 mg/mL saccharine
Applied potential or current	$E = -1.8$ V	$j = -100$ mA cm ⁻²	$j = -100$ mA cm ⁻²
Deposition time / s	1200	150	150
pH	3.65	6.25	4.00
Bath temperature / °C	25		

2.2. Structural characterization

Scanning electron microscopy (SEM) images and energy-dispersive X-ray spectroscopy (EDX) analyses were acquired using a Zeiss Merlin microscope operated at 3 kV and 15 kV, respectively. Transmission electron microscopy (TEM) and scanning transmission electron microscopy (STEM)-EDX analyses were performed on a Tecnai F20 HRTEM /STEM microscope operated at 200 kV. Cross sectional specimens were prepared by embedding the films in EPONTM epoxy resin. Subsequently, a very thin slide was cut using a microtome apparatus and placed onto a carbon-coated Cu TEM grid. $\theta/2\theta$ X-ray diffraction (XRD) patterns of the different samples were recorded on a Philips X'Pert diffractometer in the 42-54° 2θ range (step size = 0.026°, integration time = 1200 s) using Cu $K\alpha$ radiation ($\lambda = 0.1541$ nm). The crystallographic structural parameters, such as crystallite sizes, microstrains, lattice parameter and stacking fault

probability were evaluated by fitting the full XRD patterns using the Materials Analysis Using Diffraction (MAUD) Rietveld refinement program^{34,35}. Hysteresis loops were recorded at room temperature in a vibrating sample magnetometer (VSM) from Micro Sense (LOT-Quantum Design), with a maximum applied magnetic field of 4500 Oe. The loops were normalized to emu g^{-1} using the amount of material deposited as determined by coupled plasma optical emission spectroscopy (ICP-OES, model optima 4300DV). For this purpose, the films were digested in concentrated nitric acid solution at room temperature and further diluted to 1% HNO_3 .

3. Results and discussion

Nanoporous Ni, $\text{Cu}_{20}\text{Ni}_{80}$ and $\text{Cu}_{45}\text{Ni}_{55}$ (at. %) films were electrodeposited from an aqueous solution containing the metal salts and the non-ionic, amphiphilic poly(ethylene oxide)-block-poly(propylene oxide)-block-poly(ethylene oxide) (PEO-PPO-PEO) tri-block co-polymer (Pluronic[®] P-123) (Table 1). In a typical preparation, the P-123 slurry was mixed manually using a glass rod upon addition of the aqueous solution containing the metal salts. Mixing time of 1 h was required to ensure the dissolved metal species were well incorporated at the outer shell of the hydrophilic domains of the micelles. Complete mixing was confirmed by the homogeneous color and transparency of the solution. An external potential or current density was applied to reduce the metallic cations, eventually forming a silvery slab of nanoporous magnetic films (Figure 1). Hence, the surface of the working electrode acted as a solid-liquid interface, where the metallic films were deposited and patterned by the surfactant-inorganic aggregates. During the ED, the metal species are thought to move toward the working electrode together with the P-123 micelles, which act as structure-directing agents. The essence of this method is thus to

exploit the self-assembly of P-123 molecules into micelles which gather spontaneously at the solid-liquid interface during the synthesis of the mesoporous films.

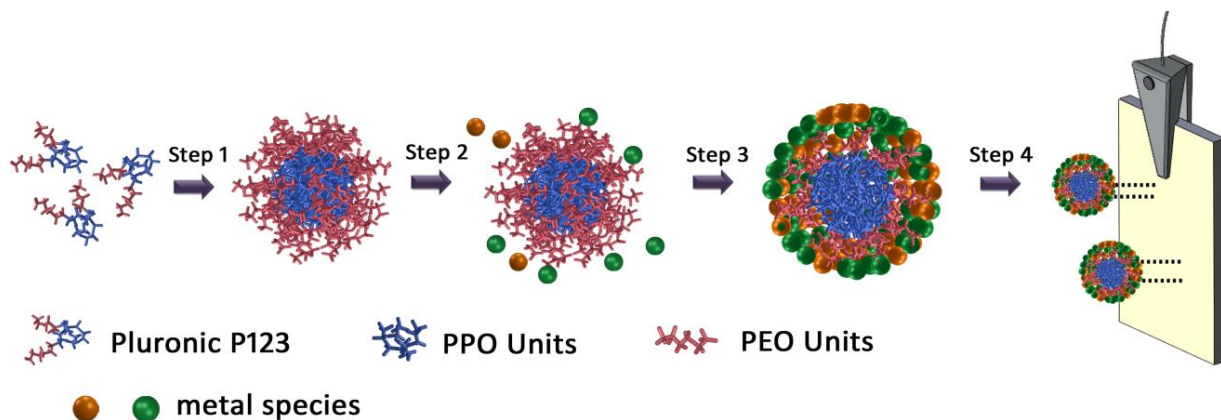


Figure 1. Schematic illustration of Pluronic P-123 micelle assembly strategy for the preparation of mesoporous magnetic films. Step 1: stirring to form the P-123 slurry; Step 2: addition of metal species to the aqueous solution; Step 3: the dissolved metal species coordinate to the PEO region of the micelles. Step 4: electrodeposition.

First, the nanoporous $\text{Cu}_{20}\text{Ni}_{80}$ film was prepared, and its surface morphology was directly observed by SEM using secondary electrons. Shown in Figure 2a is the low-magnification top view image of the film, in which a rather homogeneous nanoporosity can be distinguished. The high-magnification SEM observations (Figure 2b) demonstrate the occurrence of a hierarchical porous architecture, consisting of aggregates of nanoparticles which leave in between a high density of nanopores, whose size ranges from 5 to 10 nm. In a dilute surfactant electrolyte, as in our case, the P-123 molecules assemble into spherical micelles. A long-range organized surfactant structure does not exist, in solution because the concentration of the block copolymer is not high enough to form a lyotropic liquid crystal phase.

The interaction (electrostatic, hydrogen bonding, etc.) between metal ions and surfactant assemblies is essential to tune the arrangement of the surfactant species. Therefore, using strongly acidic or basic conditions can modify the interactions and can influence the organization of inorganic polymerizing species. Namely, the decrease of the pH of the electrolyte, from 6.25 to 4.00 (see Table 1 and Figure S1), has an impact on the morphology of the coatings. Film morphology changes from hierarchical nanoparticulated/nanoporous film to a striated patterned porous structure (Figure 2c,d). This process is probably driven by the enhanced interaction between metal ions and P-123 at a lower bath pH, which may cause alignment of the micelle spheres, ultimately resulting in the formation of a corrugated mesophase. In both cases, the concentration of surfactant was set at around 0.8 wt. % which is above the cmc of P-123 at 25 °C²⁵ but lower than the threshold for lyotropic liquid phase formation. Besides modifications in the mesopores arrangement, the composition of the film fabricated at pH = 4.00 also changed to Cu₄₅Ni₅₅. In principle, one would expect the amount of Cu in the films to diminish with a decrease in the bath pH. A simple speciation analysis of the electrolyte proves that the relative fraction of free Ni²⁺ in solution increases much faster than that of free Cu²⁺ upon lowering the pH. However, it has been demonstrated for various electrolytes that there is not a linear relationship between the percentage of Cu in the films and the pH (in the range from 4 to 9) but a minimum in the Cu content is typically observed at pH ~6^{36,37}. An increase of the copper content has been observed in acetate-based electrolytes and for C_{Ni2+} >> C_{Cu2+} when the pH is decreased from near neutral pH to 4³⁶.

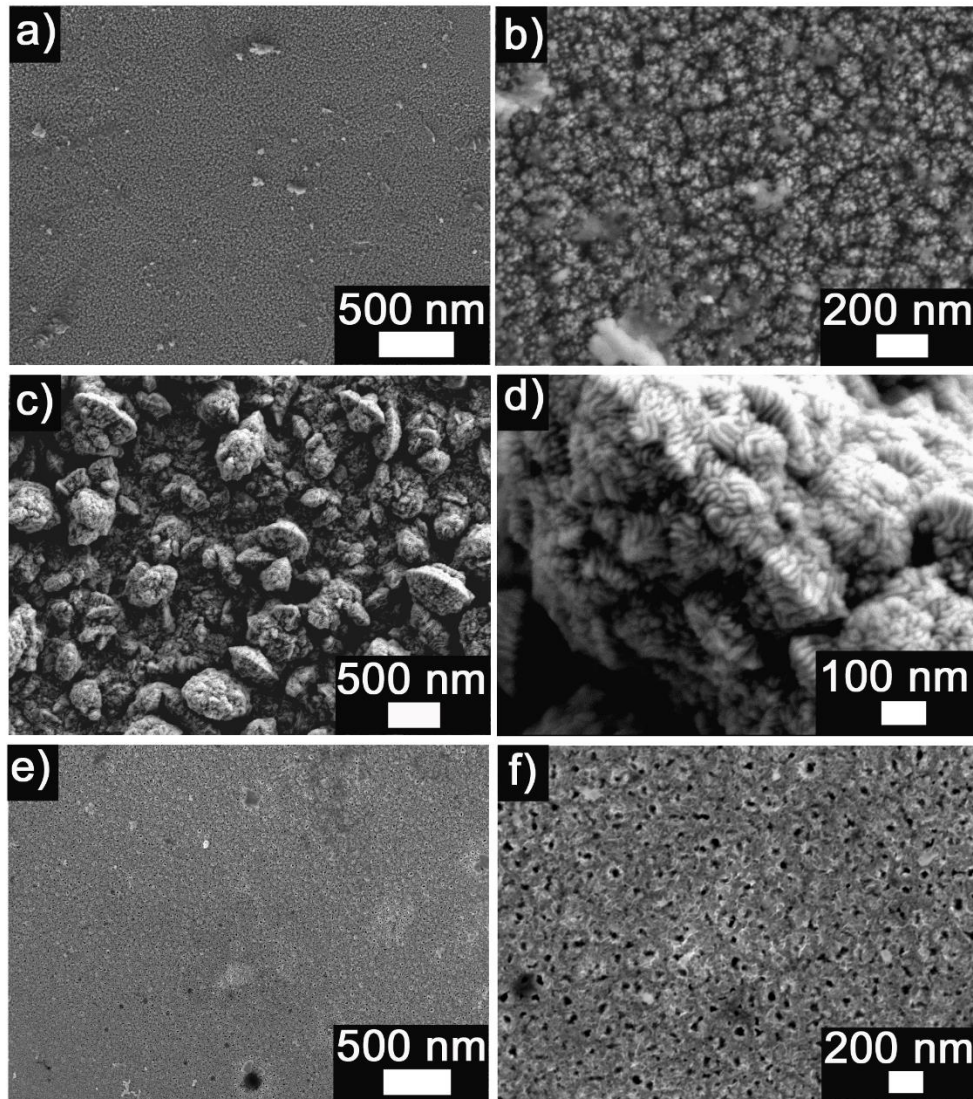


Figure 2. Low and high magnification SEM images of mesoporous: a, b) Cu₂₀Ni₈₀; c, d) Cu₄₅Ni₅₅; and e, f) Ni films.

Attempts to produce Ni films with mesoporous network from the same Cu-Ni bath were proven unsuccessful. Instead, the deposition was carried out in a more predictable way by using a ternary surfactant-cosolvent-water system. The introduction of ethanol as cosurfactant to the binary surfactant/water system enriches the aqueous P-123 phase diagram³⁸. The mesopore size is largely

determined by the hydrophobic core of the micelle spheres. The ethanol molecules are most likely anchored to the hydroxyl groups (-OH) located at the hydrophilic-hydrophobic interface, thus increasing the apparent volume of the hydrophobic blocks rather than that of the hydrophilic blocks. Thus, the ethanol cosurfactant, which acts as a swelling agent, allows for an additional control degree over the pore size^{39,40}.

As depicted in Figure 2e, the as-deposited Ni layer is homogenous and rather free from defects such as perforations or bumps. The pore connectivity is relatively low and many isolated pores can be observed (Figure 2e,f). High magnification observations reveal the occurrence of pores with on-top circular morphology, whose sizes range from 10 nm to 30 nm. As aforementioned, this increase in the pore size probably stems from the addition of the ethanol cosurfactant and the concomitant increase in the carbon chain length. In all cases, the metal species were deposited uniformly on the substrates without any cracks or voids.

To further access the inner mesoporous architecture of the films, the Cu₂₀Ni₈₀ specimen was embedded in resin and sliced in order to study its cross-section morphology. The sample was fairly robust and no obvious broken pieces were observed. The typical morphology of the cross-section of this sample, observed by SEM, is shown in Figure 3a. It is worth noting that the mesoporous structure formed on the Au cathode developed from the very initial stages of the ED process. This observation is in accordance with our preceding observations regarding the growth of pure Ni mesoporous films³⁹. Freshly formed crystallites serve as nuclei

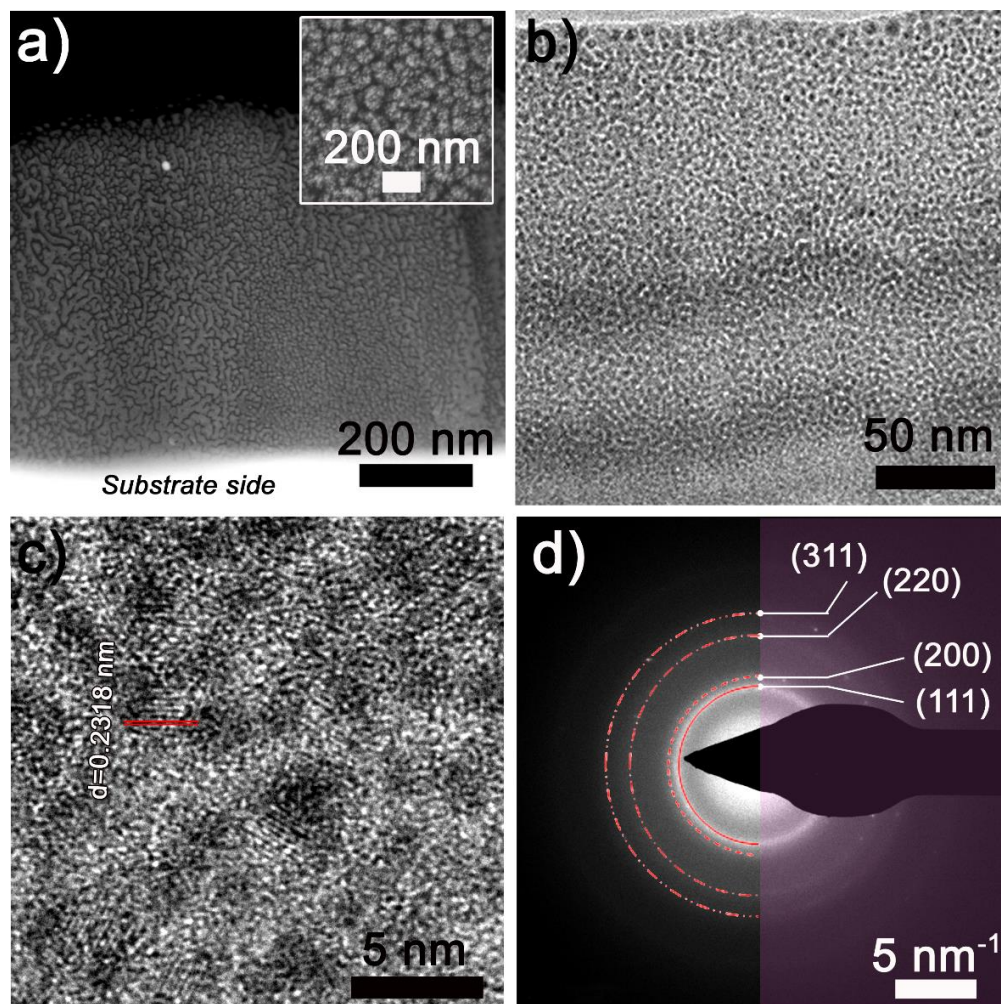


Figure 3. a) SEM, b) TEM, and c) HRTEM images of the cross-section of the mesoporous $\text{Cu}_{20}\text{Ni}_{80}$ film. The inset in a) corresponds to the on-top SEM image, for the sake of comparison; d) corresponding SAED pattern with the Miller indices of the diffracting rings.

seeds for the subsequent metallic ions discharge, hence rendering truly nanoporous sizes. TEM images demonstrate the occurrence of open-cell porosity, with highly interconnected ligaments whose lateral size is typically around 5-7 nm (Figure 3b). The high-resolution TEM (HRTEM)

image reveals that the $\text{Cu}_{20}\text{Ni}_{80}$ frameworks are highly crystalline and the lattice fringes are visible in the entire cross-section (Figure 3c). The interplanar distance seen on the image

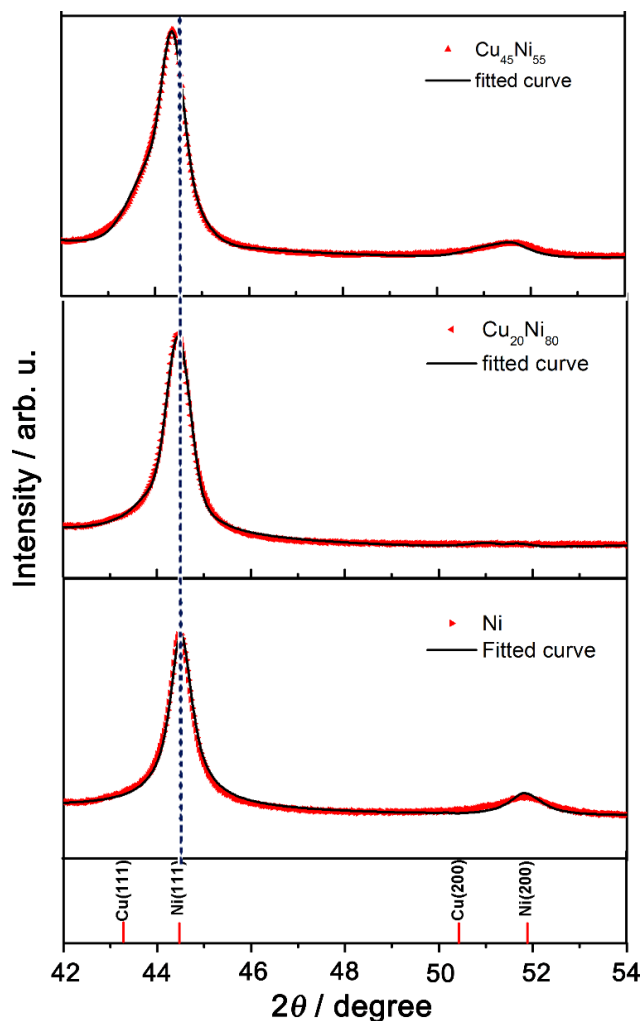


Figure 4. $\theta/2\theta$ XRD patterns in the 42° - 54° 2θ range for (► mesoporous Ni, ◄ mesoporous $\text{Cu}_{20}\text{Ni}_{80}$, ▲ mesoporous $\text{Cu}_{45}\text{Ni}_{55}$). The computed profiles (black solid lines) obtained using the MAUD program are also shown. The bottom panel shows the theoretical lines for isotropic, pure fcc Cu and Ni.

(0.2318 nm) matches the (111) planes of the face-centered cubic (fcc) structure. Figure 3d shows the corresponding selected area electron diffraction (SAED) pattern, for which the continuous rings indicate the formation of a polycrystalline material.

The crystallographic structure and phase composition of the $\text{Cu}_{45}\text{Ni}_{55}$, $\text{Cu}_{20}\text{Ni}_{80}$ and Ni films were studied by XRD (Figure 4). The most intense peaks at $44\text{-}45^\circ$ match the 2θ position expected for (111) fcc Ni and Cu-Ni solid solutions, suggesting that all the samples fully crystallize in the fcc structure (space group $\text{Fm}\bar{3}\text{m}$, as for Cu and Ni). In the case of $\text{Cu}_{20}\text{Ni}_{80}$, the (200) fcc peak, which should appear at around $2\theta = 51\text{-}52^\circ$, is not detected, suggesting a pronounced crystallographic texture along the (111) direction.

For both $\text{Cu}_{45}\text{Ni}_{55}$ and $\text{Cu}_{20}\text{Ni}_{80}$ samples, although there is no peak splitting detected, the (111) peak asymmetric broadening gives clear indication for the co-existence of Cu-rich and Ni-rich phases (*i.e.*, two fcc solid solutions with slightly different cell parameters). In order to validate this hypothesis, the Rietveld's refinement of the XRD pattern corresponding to $\text{Cu}_{45}\text{Ni}_{55}$ was performed in four different ways (Figure S2). First, the XRD pattern was fitted assuming only a single fcc solid solution without crystallographic texture (Figure S2d). Such approach did not provide a good fitting. Likewise, poor fittings were also obtained assuming a single fcc phase with (111) texture or two fcc solid solutions without texture (Figure S2b,c). Instead, a good agreement between the experimental pattern and the simulated curve was achieved upon assuming the co-existence of two fcc solutions and (111) texture (Figure S2a). In fact, phase-separation has been commonly observed for the Cu-Ni system when electrodeposition events are confined inside small cavities, as it is the case here. There are several examples in the literature (micropillars, nanowires, nanotubes) for which phase separation in Cu-Ni is observed, even in the presence of complexing agents in the electrolyte^{41,42}. Actually, the enthalpy of mixing between Ni and Cu is slightly

positive (with maximum values ranging between +0.5 to +1.5 kJ/ mol)^{43,44} Hence, there is a natural tendency for Cu and Ni to mutually segregate forming Cu-rich and Ni-rich solid solution regions when the system is brought to thermodynamical equilibrium⁴⁵.

The values of cell parameters, crystallite sizes, microstrains and stacking fault probabilities of the three samples, determined by the MAUD software, are listed in Table 2. Note that the (111) fcc main reflection shifts towards higher angles as the Cu content is decreased, suggesting an overall reduction of the lattice cell parameter (which is expectable, since the lattice constant of Ni is lower than that of Cu, and Cu-Ni alloys typically obey the Vegard's law⁴⁶). Crystallite sizes for both Ni-rich and Cu-rich solid solution phases in the Cu-Ni films are kept below 100 nm, while a value greater than 150 nm is obtained for the pure Ni film which cannot be resolved by

Table 2. Crystallographic structural parameters obtained after Rietveld's refinement of the XRD patterns of Cu₄₅Ni₅₅, Cu₂₀Ni₈₀ and Ni mesoporous films.

		Lattice parameter / Å (± 0.0005 Å)	Crystallite size / nm (± 2 nm)	Microstrains (±1.0×10 ⁻⁴)	Stacking fault probability (±0.0005)
Cu₄₅Ni₅₅	Ni-rich phase	3.5402	60	32×10 ⁻⁴	0.0058
	Cu-rich phase	3.5720	16	2×10 ⁻⁴	–
Cu₂₀Ni₈₀	Phase richer in Ni	3.5383	74	32×10 ⁻⁴	0.0067
	Phase less rich in Ni	3.5574	14	1×10 ⁻⁴	–
Ni		3.5298	> 150	9×10 ⁻⁴	0.0113

line profile analysis⁴⁷. The addition of ethanol to the Ni electrolyte lowers the dielectric constant. The decrease of conductivity of the plating solution together with the overall different bath composition induces the observed changes in crystallite size. Interestingly, particularly for the Cu-Ni mesoporous films, the crystallite size is considerably larger than the width of the pore walls, suggesting that several nanopores are contained inside coherently diffracting domains (*i.e.*, the films comprises truly nanoporous crystals rather than simply being an assembly of tiny nanoparticulate clusters). The microstrains were found to be rather low in all films, in the range of 10^{-3} and below. Saccharine is known to be an excellent tensile macrostress reducing agent and is thus responsible for the low microstrains (low density of dislocations in the crystals). The Rietveld refinement of the XRD patterns using MAUD also includes the Warren's formalism to evaluate the stacking fault (SF) probability, α_{SF} . According to the Warren's description of the SFs, $1/\alpha_{SF}$ designates the average number of planes between two consecutive SFs. Significant stacking fault probability was only found for pure Ni, and the value is around 0.0113 (Table 2), hence, there are ca. 88 planes between consecutive SFs.

The hysteresis loops of the nanoporous Cu-Ni and Ni films are shown in Figure 5. The highest value of saturation magnetization, M_S , corresponds to pure Ni while $Cu_{45}Ni_{55}$ and $Cu_{20}Ni_{80}$ films exhibit lower M_S . Interestingly, a constriction is observed in the central part of the $Cu_{20}Ni_{80}$ hysteresis loop, suggesting the presence of two magnetic phases in this sample. Taking into account the results from XRD, these two phases could be ascribed to the two fcc solid solutions indicated in Table 2. Actually, according to the Vegard's law, the two solid solutions for the $Cu_{20}Ni_{80}$ sample presumably contain about 85 at. % and 60 at. % Ni⁴⁶, hence both could show a ferromagnetic response (since the threshold for ferromagnetic behavior in Cu-Ni alloys at room temperature is indeed around 60 at. %⁴⁶). The $Cu_{45}Ni_{55}$ film does not show such narrowing of the

hysteresis, indicating the presence of a single magnetic phase. In this case, according to the Vegard's law, the Ni-rich solid solution would contain approximately 70 at. % Ni, whereas the Cu-rich phase would contain only 20 at. % Ni, hence being non-magnetic. Note also that the loop corresponding to $\text{Cu}_{20}\text{Ni}_{80}$ shows a higher remanence-to-saturation magnetization ratio (*i.e.*, a large squareness ratio, M_R/M_S). This is probably due to the in-plane shape anisotropy of this film, which is presumably fully magnetic (*i.e.*, consisting mainly of exchange coupled ferromagnetic regions). The reduction of M_R/M_S for the $\text{Cu}_{45}\text{Ni}_{55}$ film is an indication of a lower magnetic shape anisotropy (see Figure 5). This reduction of shape anisotropy is consistent with the former assumption that this film is made of Ni-rich ferromagnetic clusters embedded in a non-magnetic Cu-rich matrix (*i.e.*, a “discontinuous” magnetic structure). This non-connected magnetic structure yields to an overall decrease of exchange interactions between ferromagnetic counterparts, explaining the enhanced coercivity of the $\text{Cu}_{45}\text{Ni}_{55}$ sample with respect to the Ni film since exchange interactions are usually in detriment of the coercivity⁴⁸. Finally, the M_R/M_S value for pure Ni is also relatively low, but this could be anticipated due to its much larger thickness (7 μm , as opposed to the 600 nm – 1 μm thickness of the Cu-Ni films) and consequently lower magnetic shape anisotropy.

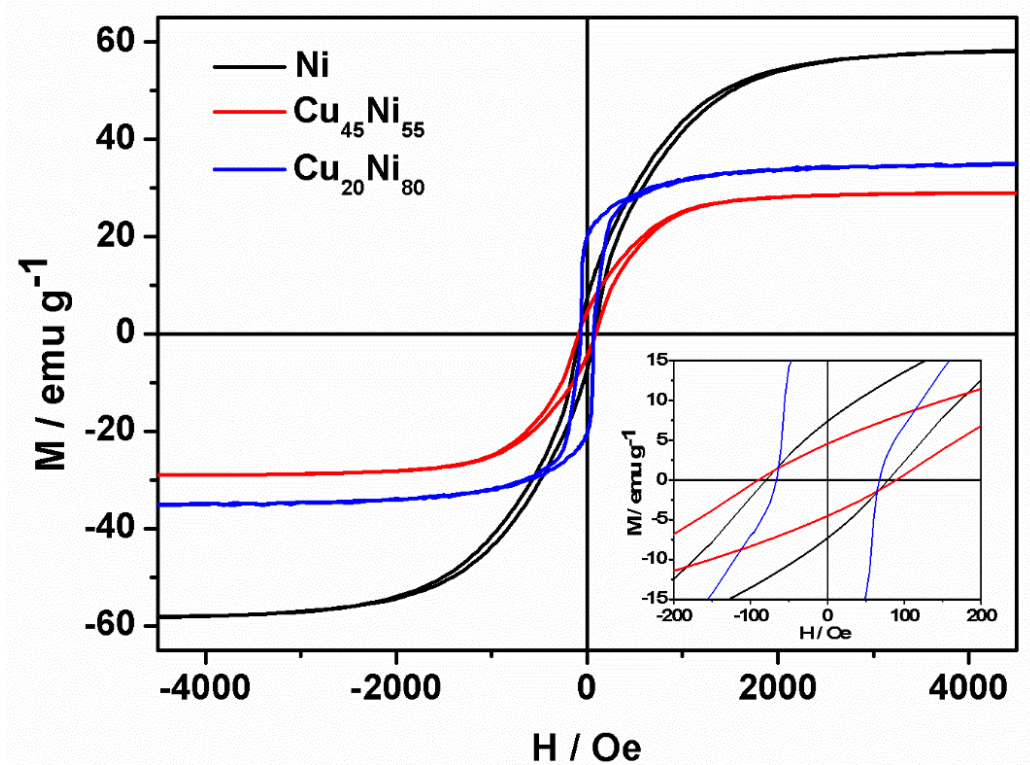


Figure 5. Room temperature hysteresis loops corresponding to Ni, Cu₄₅Ni₅₅ and Cu₂₀Ni₈₀ mesoporous films.

Mesoporous materials provide well-controlled nanosized environments where other materials with dissimilar chemical and physical properties can be hosted, leading to “nano-in-meso” multiphase composites. In this work, Al₂O₃, which is the most widely studied material of those prepared by ALD, was chosen to coat and fill the pores of the Cu₂₀Ni₈₀ films. A Cu₂₀Ni₈₀/Al₂O₃ specimen was prepared for cross-sectional imaging to assess the quality of the oxide nanocoating. After the ALD process, as shown in the STEM image (Figure 6a), the Cu₂₀Ni₈₀ alloy, featuring a brighter contrast, is covered by a darker-contrast layer. The composition profile across the interface was determined by STEM-EDX elemental distribution mapping. The analysis reveals that the local distribution of Al (in red) and Ni (in green) elements is well-distinguished and that the irregular border between the two elemental maps follows the surface geometry, hence pointing to a

conformal coating of Al_2O_3 . However, there is not such a clear compositional distinction between the O and Ni signals but, instead, they co-exist within a few nanometers interval. This was further proved by performing a STEM-EDX line scan analysis (Figure 6b). When the electron beam was swept from the outer surface of the film towards the inner part of the material (vertical arrow in the scheme), the Al and O signals first appear at 20 nm from the starting point and vanish at approximately 90 nm. The Cu and Ni signals monotonically increase from around 35 nm, suggesting that the thickness of the Al_2O_3 coating is about 50 nm. Hence, there is not an abrupt switch in composition but rather the four elements are present within a distance of about 55 nm from the upper surface. Therefore, it is conjectured that the outermost surface of mesoporous Cu-Ni films got slightly oxidized during the ALD process, which is plausible bearing in mind that such treatments are performed under O_3 atmosphere. Hence, Ni-oxide, Cu-oxide and some mixed $(\text{Al,Cu,Ni})_x\text{O}_y$ phases may exist within this region.

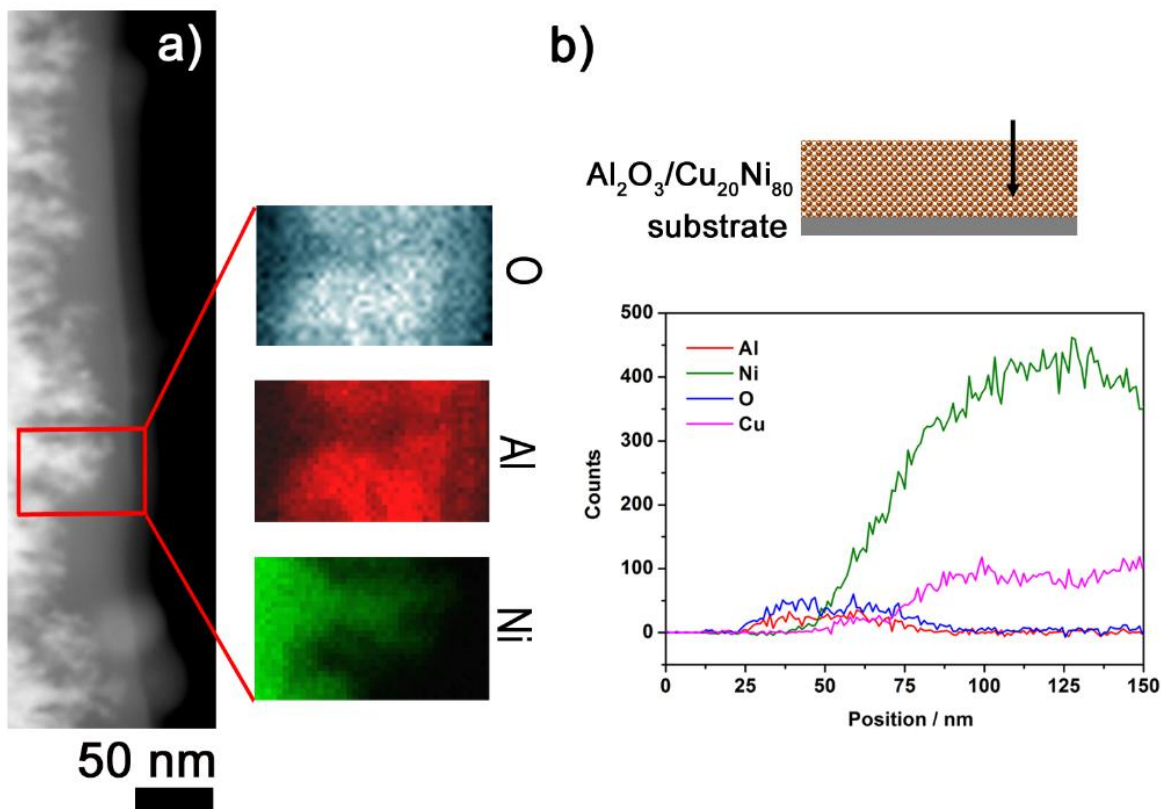


Figure 6. a) STEM image and EDX elemental distribution of O, Al and Ni in the interfacial area enclosed within the red rectangle for a cross-sectioned Al₂O₃/Cu₂₀Ni₈₀ film; b) EDX line scan performed across the interface between Cu₂₀Ni₈₀ and Al₂O₃, as indicated by the arrow in the scheme shown above.

XRD patterns were recorded to confirm the formation of oxidized Cu-Ni phases and to assess whether the ALD treatments could have induced further phase separation, as previously reported in fully-dense Cu-Ni films subject to annealing treatments⁴⁵. As depicted in Figure 7a, a small peak appears after ALD at around $2\theta = 43^\circ$, which can be ascribed to Cu- or Ni-oxides. However, no obvious change of the (111) fcc reflections is observed (no peak splitting or further asymmetric shape), suggesting that the Cu-Ni mesoporous films can withstand the ALD process to a great extent from both morphological and crystallographic aspects. This could be anticipated since phase separation in electrodeposited Cu-Ni films was observed above 250 °C⁴⁵. Only a narrowing of the (111) peak occurs, which is indicative of grain growth and reduction of residual stresses caused by the annealing process which accompanies the ALD process (crystallite size after the ALD treatment is larger than 150 nm and cannot be resolved by X-ray line profile analysis, as evaluated using MAUD).

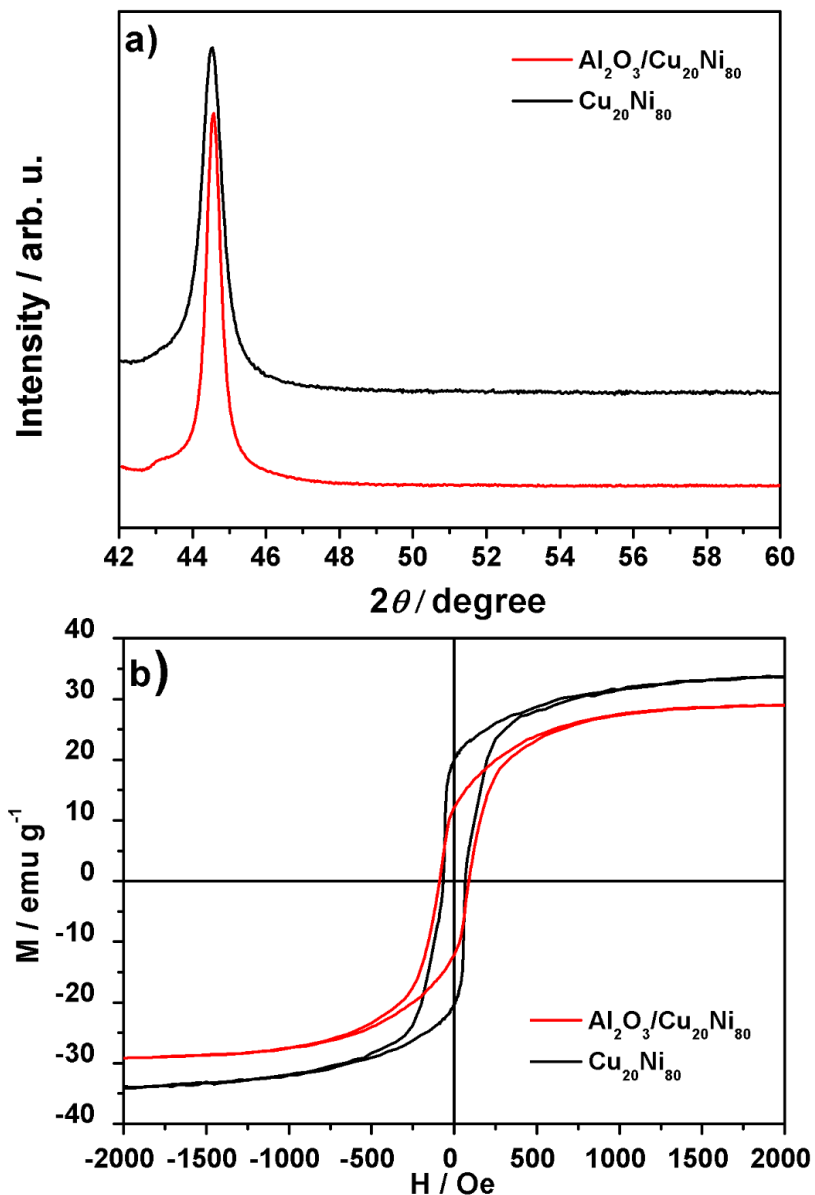


Figure 7. a) XRD patterns and b) room temperature hysteresis loops of mesoporous $\text{Cu}_{20}\text{Ni}_{80}$ and $\text{Al}_2\text{O}_3@\text{Cu}_{20}\text{Ni}_{80}$ composite films.

No peaks corresponding to crystalline Al_2O_3 are observed in the measured 2θ range. This is in agreement with the formation of amorphous Al_2O_3 by ALD, as previously reported in the literature when similar ALD conditions are employed³³. Finally, due to the slight oxidation that takes place

during ALD, the saturation magnetization is found to decrease (Figure 7b) but only by 15%, hence a clear ferromagnetic response is preserved.

4. Conclusions

This work demonstrates the possibility to grow Ni and Cu-Ni mesoporous metallic films, with highly tunable pore architectures, compositions and magnetic properties, by ED in the presence of a tri-block copolymer surfactant. Nanopores well distributed both throughout the surface and within the films were observed. The mesoporous films can serve as scaffolds and be successfully coated with Al₂O₃ nanolayers by atomic layer deposition. This has been proven on the Cu₂₀Ni₈₀ film. Although some surface oxidation occurs during the ALD process, both the crystallographic structure and the parent magnetic properties of the metallic matrix are greatly preserved. Hence, the concept exploited here can render functional multiphase metal-ceramic nanocomposites which are entirely processed using a chemical-like route: electrochemical deposition followed by a subclass of chemical vapor deposition (ALD). These “nano-in-meso” composites could find applications in several fields like magnetic MEMS/NEMS or protective coatings.

ASSOCIATED CONTENT

Supporting information

Additional EDX spectra and Rietveld fitted XRD patterns are available in the S.I.

AUTHOR INFORMATION

Corresponding Author

* jinzhang@nwpu.edu.cn

* eva.pellicer@uab.cat

* jordi.sort@uab.cat

Author Contributions

The manuscript was written through contributions of all authors. All authors have given approval to the final version of the manuscript.

ACKNOWLEDGMENTS

Financial support by the European Research Council (SPIN-PORICS 2014-Consolidator Grant, Agreement N° 648454), the Spanish Government (Project MAT2017-86357-C3-1-R and associated FEDER) and the “Severo Ochoa” Programme for Centres of Excellence in R& D (SEV-2015-0496), the Generalitat de Catalunya (2014-SGR-1015) and the European Union’s Horizon 2020 research and innovation programme under the Marie Skłodowska-Curie grant agreement n° 665919 is acknowledged. E.P. and M. C. are grateful to MINECO for the “Ramón y Cajal” contract (RYC-2012-10839 and RYC-2013-12448).

REFERENCES

- (1) Yamauchi, Y.; Suzuki, N.; Radhakrishnan, L.; Wang, L. Breakthrough and Future: Nanoscale Control of Compositions, Morphologies, and Mesochannel Orientations toward Advanced Mesoporous Materials. *Chem. Rec.* **2009**, *9*, 321-339.
- (2) Corma, A. From Microporous to Mesoporous Molecular Sieve Materials and Their Use in Catalysis. *Chem. Rev.* **1997**, *97*, 2373-2419.
- (3) Ying, J. Y.; Mehnert, C. P.; Wong, M. S. Synthesis and Applications of Supramolecular-Templated Mesoporous Materials. *Angew. Chem., Int. Ed.* **1999**, *38*, 56-77.
- (4) Davis, M. E. Ordered Porous Materials for Emerging Applications. *Nature* **2002**, *417*, 813-821.
- (5) Soler-Illia, G. J. A. A.; Azzaroni, O. Multifunctional Hybrids by Combining Ordered Mesoporous Materials and Macromolecular Building Blocks. *Chem. Soc. Rev.* **2011**, *40*, 1107-1150.
- (6) Boissiere, C.; Grosso, D.; Chaumonnot, A.; Nicole, L.; Sanchez, C. Aerosol Route to Functional Nanostructured Inorganic and Hybrid Porous Materials. *Adv. Mater.* **2011**, *23*, 599-623.
- (7) Liu, J.; Qiao, S. Z.; Hu, Q. H.; Lu, G. Q. Magnetic Nanocomposites with Mesoporous Structures: Synthesis and Applications. *Small* **2011**, *7*, 425-443.
- (8) Scaglione, F.; Rizzi, P.; Battezzati, L. De-alloying Kinetics of an Au-based Amorphous Alloys. *J. Alloys Compd.* **2012**, *536*, S60-S64.

(9) Bansal, V.; Jani, H.; Du Plessis, J.; Coloe, P. J.; Bhargava, S. K. Galvanic Replacement Reaction on Metal Films: A One-Step Approach to Create Nanoporous Surfaces for Catalysis. *Adv. Mater.* **2008**, *20*, 717-723.

(10) Attard, G. S.; Glyde, J. C.; Göltner, C. G. Liquid-crystalline Phases as Templates for the synthesis of Mesoporous Silica. *Nature* **1995**, *378*, 366-368.

(11) Attard, G. S.; Göltner, C. G.; Corker, J. M.; Henke, S.; Templer, R. H. Liquid-Crystal Templates for Nanostructured Metals. *Angew. Chem., Int. Ed. Engl.* **1997**, *36*, 1315-1317.

(12) Attard, G. S.; Bartlett, P. N.; Coleman, N. R. B.; Elliott, J. M.; Owen, J. R.; Wang, J. H. Mesoporous Platinum Films from Lyotropic Liquid Crystalline Phases. *Science* **1997**, *278*, 838-840.

(13) Wang, H.; Jeong, H. Y.; Imura, M.; Wang, L.; Radhakrishnan, L.; Fujita, N.; Castle, T.; Terasaki, O.; Yamauchi, Y. Shape- and Size-Controlled Synthesis in Hard Templates: Sophisticated Chemical Reduction for Mesoporous Monocrystalline Platinum Nanoparticles. *J. Am. Chem. Soc.* **2011**, *133*, 14526-14529.

(14) Choi, K. S.; McFarland, W.; Stucky, G. D. Electrocatalytic Properties of Thin Mesoporous Platinum Films Synthesized Utilizing Potential-Controlled Surfactant Assembly. *Adv. Mater.* **2013**, *15*, 2018-2021.

(15) Malgras, V.; Araee-Esfahani, H.; Wang, H.; Jiang, B.; Li, C.; Wu, K. C. W.; Kim, J. H.; Yamauchi, Y. Nanoarchitectures for Mesoporous Metal. *Adv. Mater.* **2016**, *28*, 993-1010.

(16) Li, C.; Dag, O.; Dao, T. D.; Nagao, T.; Sakamoto, Y.; Kimura, T.; Terasaki, O.; Yamauchi, Y. Electrochemical Synthesis of Mesoporous Gold Films toward Mesospace-stimulated Optical Properties. *Nature Commun.* **2015**, *6*, 6608.

(17) Iqbal, M.; Li, C.; Wood, K.; Jiang, B.; Takei, T.; Dag, O.; Baba, D.; Nugraha, A. S.; Asahi, T.; Whitten, A. E.; Hossain, Md. S. A.; Malgras, V.; Yamauchi, Y. Continuous Mesoporous Pd Films by Electrochemical Deposition in Nonionic Micellar Solution. *Chem. Mater.* **2017**, *29*, 6405-6413.

(18) Wang, H.; Wang, L.; Sato, T.; Sakamoto, Y.; Tominaka, S.; Miyasaka, K.; Miyamoto, N.; Nemoto, Y.; Terasaki, O.; Yamauchi, Y. Synthesis of Mesoporous Pt Films with Tunable Pore Sizes from Aqueous Surfactant Solutions. *Chem. Mater.* **2012**, *24*, 1591-1598.

(19) Li, C.; Jiang, B.; Wang, Z.; Li, Y.; Hossain, Md. S. A.; Kim, J. H.; Takei, T.; Henzie, J.; Dag, O.; Bando, Y.; Yamauchi, Y. First Synthesis of Continuous Mesoporous Copper Films with Uniformly Sized Pores by Electrochemical Soft Templating. *Angew. Chem. Int. Ed.* **2016**, *128*, 12938-12942.

(20) Li, C.; Yamauchi, Y.; Synthesis of Mesoporous Platinum–Copper Films by Electrochemical Micelle Assembly and Their Electrochemical Applications. *Chem. Eur. J.* **2014**, *20*, 729-733.

(21) Isarain-Chavez, E.; Baró, M. D.; Pellicer, E.; Sort, J.; Micelle-assisted Electrodeposition of Highly Mesoporous Fe–Pt Nodular Films with Soft Magnetic and Electrocatalytic Properties. *Nanoscale* **2017**, *9*, 18081-18093.

(22) Isarain-Chavez, E.; Baró, M. D.; Alcantara, C.; Pané, S.; Sort, J.; Pellicer, E. Micelle-Assisted Electrodeposition of Mesoporous Fe-Pt Smooth Thin Films and their Electrocatalytic Activity towards the Hydrogen Evolution Reaction. *ChemSusChem* **2018**, *11*, 367-375.

(23) Wang, H.; Imura, M.; Nemoto, Y.; Wang, L.; Jeong, H. Y.; Yokoshima, T.; Terasaki, O.; Yamauchi, Y. Electrochemical Design of Mesoporous Pt-Ru Alloy Films with Various Compositions toward Superior Electrocatalytic Performance. *Chem. Eur. J.* **2012**, *18*, 13142-13148.

(24) Quintana, A.; Zhang, J.; Chavaz, E. I.; Menendez, E.; Cuadrado, R.; Robles, R.; Baró, M. D.; Guerrero, M.; Pané, S.; Nelson, B. J.; Muller, C. M.; Ordejon, P.; Nogués, J.; Pellicer, E.; Sort, J. Magnetic actuation: Voltage-induced Coercivity Reduction in Nanoporous Alloy Films: A Boost towards Energy Efficient Magnetic Actuation. *Adv. Funct. Mater.* **2017**, *27*, 1701904.

(25) Wanka, G.; Hoffmann, H.; Ulbricht, W. Phase Diagrams and Aggregation Behavior of Poly (ox yethylene)-Poly (oxypropylene) -Poly(oxyet hylene) Triblock Copolymers in Aqueous Solutions. *Macromolecules* **1994**, *27*, 4145-4159.

(26) Hellman, F.; Hoffmann, A.; Tserkovnyak, Y.; Beach, G. S. D.; Fullerton, E. E.; Leighton, C.; MacDonald, A. H.; Ralph, D. C.; Arena, D. A.; Dürr, H. A.; Fischer, P.; Grollier, J.; Heremans, J. P.; Jungwirth, T.; Kimel, A. V.; Koopmans, B.; Krivorotov, I. N.; May, S. J.; Petford-Long, A. K.; Rondinelli, J. M.; Samarth, N.; Schuller, I. K.; Slavin, A. N.; Stiles, M. D.; Tchernyshyov, O.; Thiaville, A.; Zink, B. L. Interface-induced Phenomena in Magnetism. *Rev. Mod. Phys.* **2017**, *89*, 025006.

(27) Liu, J.; Qiao, S. Z.; Hu, Q. H.; Lu, G. Q. Magnetic Nanocomposites with Mesoporous Structures: Synthesis and Applications. *Small* **2011**, *7*, 425-443.

(28) Xia, X. H.; Tu, J. P.; Zhang, Y. Q.; Mai, Y. J.; Wang, X. L.; Gu, C. D.; Zhao, X. B. Three-Dimensional Porous Nano-Ni/Co(OH)₂ Nanoflake Composite Film: A Pseudocapacitive Material with Superior Performance. *J. Phys. Chem. C*, **2011**, *115*, 22662.

(29) Zhang, Y. Q.; Xia, X. H.; Wang, X. L.; Mai, Y. J.; Shi, S. J.; Tang, Y. Y.; Gu, C. G.; Tu, J. P. Three-dimensional Porous Nano-Ni Supported Silicon Composite Film for High-performance Lithium-ion Batteries. *J. Power Source*, **2012**, *213*, 106-111.

(30) Detavernier, C.; Dendooven, J.; Sree, S. P.; Ludwig, K. F.; Martens, J. A. Tailoring Nanoporous Materials by Atomic Layer Deposition. *Chem. Soc. Rev.*, **2011**, *40*, 5242-5253

(31) Elam, J. W.; Xiong, G.; Han, C. Y.; Wang, H. H.; Birrell, J. P.; Welp, U.; Hryn, J. N.; Pellin, M. J.; Baumann, T. F.; Poco, J. F.; Satcher, J. H. Atomic layer deposition for conformal coating of nanoporous materials. *J. Nanomater.*, **2006**, 64501,1-5.

(32) Spende, A.; Sobel, N.; Lukas M.; Zierold, R.; Riedl, J. C.; Gura, L.; Schubert, I.; Montero-Moreno, J. M.; Nielsch, K.; Stühn, B. TiO₂, SiO₂, and Al₂O₃ Coated Nanopores and Nanotubes Produced by ALD in Etched Ion-Track Membranes for Transport Measurements. *Nanotechnology*, **2015**, *26*, 335301.

(33) Zhang, J.; Coll, M.; Puig, T.; Pellicer, E.; Sort, J. Conformal Oxide Nanocoatings on Electrodeposited 3D Porous Ni Films by Atomic Layer Deposition *J. Mater. Chem. C* **2016**, *4*, 8655-8622.

(34) Lutterotti, L.; Scardi, P. Simultaneous Structure and Size-strain Refinement by the Rietveld Method. *J. Appl. Cryst.* **1990**, *23*, 246-252.

(35) MAUD (Materials Analysis Using Diffraction), <http://maud.radiographema.com/>.

- (36) Silaimani, S. M.; Vivekanandan, G.; Veeramani, P. Nano-Nickel–Copper Alloy Deposit for Improved Corrosion Resistance in Marine Environment. *Int. J. Environ. Sci. Technol.* **2015**, *12*, 2299–2306.
- (37) Sobha, J.; Krishna, N.; Sujatha, K. P.; Sriveeraraghavan, S.; Krishnan, R. M.; Natarajan, S. R. Electroplating of nickel-copper alloys. *Bull. Electrochem.* **1996**, *12*, 259–265.
- (38) Soni, S. S.; Brotons, G.; Bellour, M.; Narayanan, T.; Gibaud, A.; Quantitative SAXS Analysis of the P123/Water/Ethanol Ternary Phase Diagram. *J. Phys. Chem. B* **2006**, *110*, 15157-15165.
- (39) Esque-de los Ojos, D.; Zhang, J.; Fornell, J.; Pellicer, E.; Sort, J.; Nanomechanical Behaviour of Open-cell Nanoporous Metals: Homogeneous versus Thickness-dependent Porosity. *Mech. Mater.* **2016**, *100*, 167-174.
- (40) Holmqvist, P.; Alexandridis, P.; Lindman, B. Phase Behavior and Structure of Ternary Amphiphilic Block Copolymer–Alkanol–Water Systems: Comparison of Poly(ethylene oxide)/Poly(propylene oxide) to Poly(ethylene oxide)/Poly(tetrahydrofuran) Copolymers. *Langmuir* **1997**, *13*, 2471-2479.
- (41) Varea, A.; Pané, S.; Gerstl, S.; Zeeshan, M. A.; Özkale, B.; Nelson, B. J.; Suriñach, S.; Baró, M. D.; Nogués, J.; Sort, J.; Pellicer E. Ordered Arrays of Ferromagnetic, Compositionally Graded $\text{Cu}_{1-x}\text{Ni}_x$ Alloy Nanopillars Prepared by Template-Assisted Electrodeposition. *J. Mater. Chem. C* **2013**, *1*, 7215-7221.
- (42) Liu, Z.; Elbert, D.; Chien, C. L.; Searson, P. C. FIB/TEM Characterization of the Composition and Structure of Core/Shell Cu–Ni Nanowires. *Nano Lett.* **2008**, *8*, 2166-2170.

(43) Abrikosov, I. A.; Skriver, H. L. Self-Consistent Linear-Muffin-Tin-Orbitals Coherent-Potential Technique for Bulk and Surface Calculations: Cu-Ni, Ag-Pd, and Au-Pt Random Alloys. *Phys. Rev. B* **1993**, *47*, 16532-16541.

(44) Lee, B. J.; Shim, J. H. A Modified Embedded Atom Method Interatomic Potential for the Cu–Ni System. *Calphad* **2004**, *28*, 125-132.

(45) Pellicer, E.; Varea, A.; Kartik, S.; Pané, S.; Suriñach, S.; Baró, M. D.; Nogués, J.; Nelson, B.; Sort, J. Grain Boundary Segregation and Interdiffusion Effects in Nickel–Copper Alloys: An Effective Means to Improve the Thermal Stability of Nanocrystalline Nickel. *ACS Appl. Mater. Interf.* **2011**, *3*, 2265-2274.

(46) Pellicer, E.; Varea, A.; Pané, S.; Nelson, B. J.; Menéndez, E.; Estrader, M.; Suriñach, S.; Baró, M. D.; Nogués, J.; Sort, J. Nanocrystalline Electroplated Cu-Ni: Metallic Thin Films with Enhanced Mechanical Properties and Tunable Magnetic Behavior. *Adv. Funct. Mater.* **2010**, *20*, 983-991.

(47) Cullity, B. D. *Elements of X-ray Diffraction*; Addison- Wesley Publishing Company, Inc.: Reading, Massachusetts, USA, 1956, p. 262.

(48) Chikazumi, S. *Physics of Magnetism*; John Wiley & Sons, Inc.: USA, 1964, p. 254.

Table of Contents Graphic

